RSC Advances

PAPER

View Article Online
View Journal | View Issue

Cite this: *RSC Adv.*, 2017, **7**, 3783

Al^{3+}-Induced growth of α-$Co(OH)_2$ nanoplates as high-capacity supercapacitors and water oxidation electrocatalysts†

Rongmei Liu,*[a] Zixiang Jiang,[a] Juping Ma,[a] Lu Ni,[a] Xueying Sun,[a] Yong Liu,[a] Haixing Chen[a] and Qi Liu[b]

Received 2nd November 2016
Accepted 17th December 2016

DOI: 10.1039/c6ra26160d

www.rsc.org/advances

In this paper, we report a metal ion-induced synthesis of α-$Co(OH)_2$ nanoplates as high-capacity supercapacitors and water oxidation electrocatalysts, which were synthesized by using metal ions of Al^{3+} as a structure-inducing agent through hydrothermal treatment. When used as electrode materials in supercapacitors, α-$Co(OH)_2$ nanoplates exhibit good capacitive properties of 709.1 F g^{-1} at a current density of 1 A g^{-1}, maintaining 95.8% of the initial capacity at the current density of 5 A g^{-1} after 1000 cycles. The α-$Co(OH)_2$ nanoplates can effectively oxidize water, showing excellent OER activity with a small overpotential of 348 mV at the current density of 10 mA cm^{-2} and a large mass activity of 28.2 A g^{-1}, much higher than that of the β-$Co(OH)_2$ particle electrocatalyst (0.2 A g^{-1}). These results provide a new and facile approach to fabricating high-performance electrodes for supercapacitors and water oxidation electrocatalysts.

Introduction

Cobalt hydroxide, one of the most competitive electrode materials for next-generation high-performance supercapacitors and water oxidation electrocatalysts, has been widely researched for its unique layer structure, excellent electrochemical property, low cost and environment-friendliness.[1–5] However, as supercapacitors, the experimental specific capacitances of prepared $Co(OH)_2$ electrodes are much lower than the theoretical value, and they have poor cycle stability.[6–8] Thus, it is a big challenge for scientists to improve the experimental specific capacitance and cycle stability of $Co(OH)_2$ electrodes. An effective water oxidation electrocatalyst that can speed up the reaction, decrease the overpotential, and thus enhance the energy conversion efficiency is highly desired.[9,10]

As is well-known, materials' properties depend greatly on their size, shape and crystal structure; therefore, the control of the shape/structure of materials has become one of the hottest topics in materials science.[11–14] During crystal growth, the shape evolution is principally driven by the growth environment. Thus, the species in the growth environment play important roles; introducing additives into the synthesis system may be an effective way to induce some new shapes with abundant crystal defects, since the additive would possibly interact with some atomic configurations to change the relative surface stability.[15–19] Crystals with abundant defects are beneficial in improving the electrochemical performance in terms of pseudocapacitance and the electrocatalysis of water. Moreover, the sheet or plate-like structures of $Co(OH)_2$ can provide large intersheet spacing for transferring the ions rapidly and increasing the electroactive material–electrolyte interface area.[20–24] Therefore, many attempts have been applied for the synthesis of layered nanostructures of $Co(OH)_2$ with abundant defects. It has been found that substitution of the cobalt ions by other metal ions can produce multi-phase metal oxides/hydroxides and introduce abundant structural defects.[25–28] Theoretically, the incorporation of inactive metal ions into the lattice can stabilize the crystal structure of α-$Co(OH)_2$ during the electrode reactions. Thus, the capacitance properties and cycle stability of the α-$Co(OH)_2$ electrode are expected to be improved significantly. Tang *et al.* have synthesized interconnected Zn-substituted α-$Co(OH)_2$ nanosheets on nickel foam substrates with good cycle ability through the electrochemical deposition method.[26] Gupta *et al.* have synthesized Al-substituted α-$Co(OH)_2$ on stainless steel electrodes by a potentiostatic deposition process.[27] All these efforts employ electrochemical deposition; there are very few reports that use the solution method for synthesis of plate-like Al-substituted α-$Co(OH)_2$.

In this paper, we provide a new method for the controllable synthesis of α-$Co(OH)_2$ nanoplates by using Al^{3+} metal ions as structure-inducing agents and ammonium solution as the alkali source through a hydrothermal method. The electrochemical

[a]College of Biological and Chemical Engineering, Anhui Polytechnic University, Wuhu, Anhui 241000, P. R. China. E-mail: liurongmei@ahpu.edu.cn; Fax: +86 553 2871 255; Tel: +86 553 2871 255

[b]College of Materials Science and Engineering, Anhui Polytechnic University, Wuhu, Anhui 241000, P. R. China

† Electronic supplementary information (ESI) available. See DOI: 10.1039/c6ra26160d

performance of as-prepared α-$Co(OH)_2$ nanoplates as electrode materials for supercapacitors and as water oxidation electrocatalysts were systematically measured.

Results and discussion

Fig. 1a shows the XRD pattern of the as-prepared sample controlled by Al^{3+} ions. All the diffraction peaks can be indexed to the standard crystallographic spectrum of the layered α-$Co(OH)_2$ (JCPDS: 46-0605),[26,29] indicating that pure α-$Co(OH)_2$ products were obtained under the synthetic conditions, the octahedral Co^{2+} ions were partially substituted by Al^{3+} ions, the incorporated Al^{3+} ions did not obviously change the crystal structure of α-$Co(OH)_2$, and the layered α-$Co(OH)_2$ was prepared.

As Al^{3+} ions were used in the reaction system, X-ray photoelectron spectroscopy (XPS) was used to identify the content of Al element. Fig. 2a shows the spectrum of the sample, indicating the presence of Co, Al and O elements. The high-resolution XPS spectrum shown in Fig. 2b gives the binding energies of Al 2p, corresponding to 75.02 eV, with weak intensity. Fig. 2c presents the binding energies of Co $2p_{3/2}$ and Co $2p_{1/2}$, at 782.2 and 798.2 eV. The atomic concentrations of O 1s, Co 2p and Al 2p obtained by XPS are 41.67%, 11.85% and 6.31%, respectively, which shows that the Al/Co atomic ratio in α-$Co(OH)_2$ nanoplates is 53.25%. We also measured the contents of Al and Co element in α-$Co(OH)_2$ nanoplates by inductively coupled plasma spectroscopy (ICP), and the results show that the Al/Co atomic ratio in α-$Co(OH)_2$ nanoplates is 21.56%. These results suggest that the Al content on the surface is much higher than that in the body of α-$Co(OH)_2$ nanoplates, since XPS provides the information for the top layers (1–10 nm) of the surface. They confirm that Al^{3+} ions would partially occupy the position of Co^{2+} ions and direct the growth to form plate-like α-$Co(OH)_2$ nanocrystals. The sample's Raman spectrum is shown in Fig. S1.†

Fig. 3a–c show scanning electron microscope (SEM) and transmission electron microscope (TEM) images of the

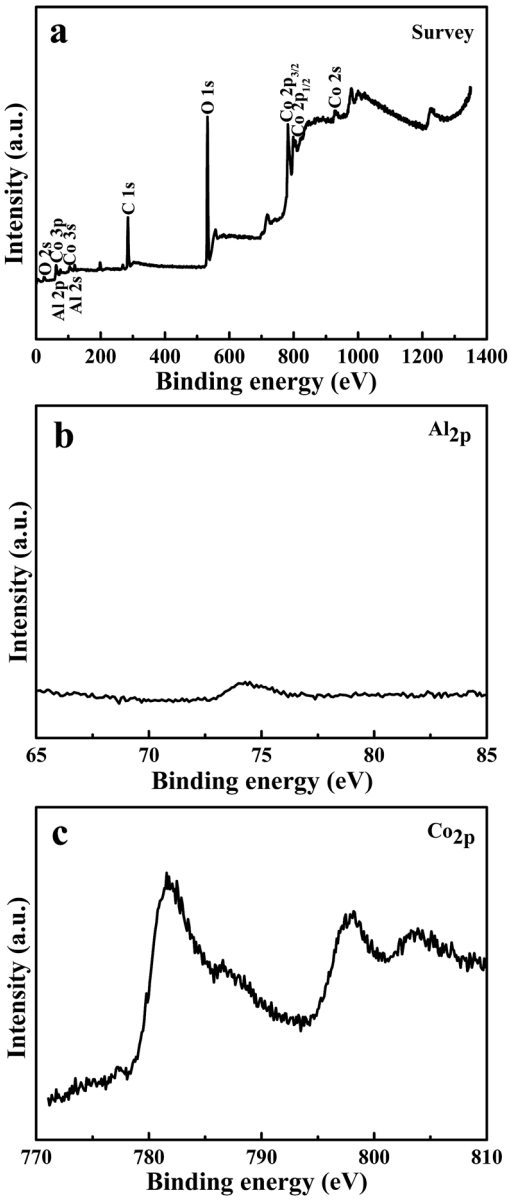

Fig. 2 (a) XPS spectra, (b) Al 2p and (c) Co 2p spectrum of the obtained sample controlled by $AlCl_3$.

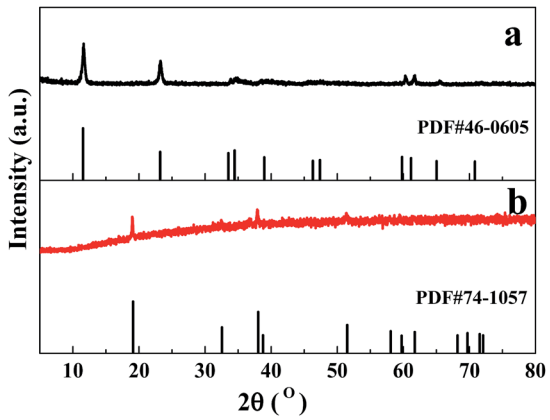

Fig. 1 XRD patterns of (a) the as-prepared sample controlled by $AlCl_3$ and (b) the sample synthesized without $AlCl_3$; vertical marks correspond to the standard XRD pattern for α-$Co(OH)_2$ and β-$Co(OH)_2$.

obtained α-$Co(OH)_2$ sample controlled by Al^{3+} ions. As shown in Fig. 3a and b, the majority of the sample comprises plate-like nanocrystals. From the high-magnification SEM images shown in Fig. 3c, it can be seen that these nanoplates are about 200 nm in side length and several nanometers in thickness and are generally hexagonal in shape. Fig. 3d–f show the sample's TEM images and the HRTEM image with SAED pattern. The TEM images also confirm that majority of the obtained sample has a hexagonal shape with a side length of about 200 nm. The HRTEM image (Fig. 3f) of a hexagonal nanoplate shows one set of lattice fringes with interplanar distance of 2.7 Å, corresponding to the (100) plane. Similar results are obtained from the SAED pattern with a perfect hexagonal spot pattern as shown in Fig. 3f inset. Thus, the HRTEM image of the hexagonal planar nanocrystal is projected from the [001] zone axis.

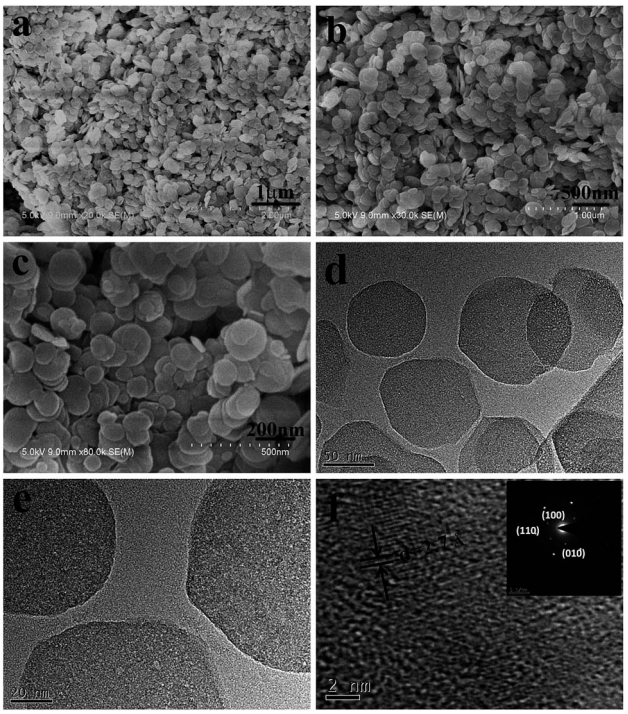

Fig. 3 (a–c) SEM images, (d and e) TEM image and (f) HRTEM image along with the SAED pattern (inset) of α-$Co(OH)_2$ nanoplates.

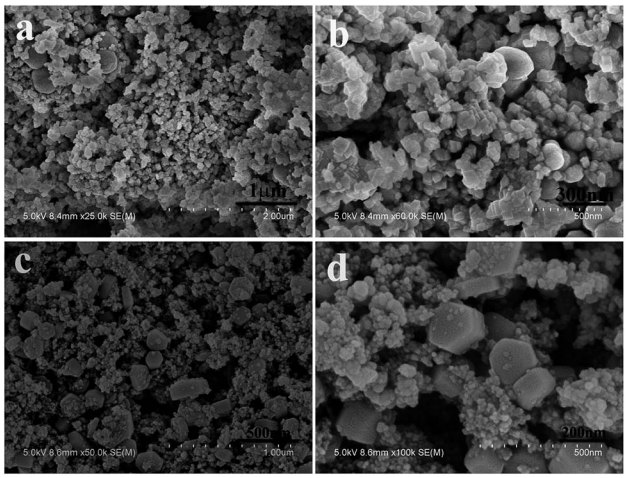

Fig. 4 SEM images of (a and b) the sample without $AlCl_3$ and (c and d) the sample controlled by NaCl.

In the reaction system, Al^{3+} ions may be the reason for the formation of α-$Co(OH)_2$ nanoplates. Without the addition of $AlCl_3$, when only the mixture of $CoAc_2$ and ammonium solution was hydrothermally treated, as shown in Fig. 4a and b, only irregular particles and microplates were obtained. The sample's XRD pattern is shown in Fig. 1b; all the diffraction peaks can be indexed to the standard crystallographic spectrum of β-$Co(OH)_2$ (JCPDS: 74-1057),[20] indicating that pure β-$Co(OH)_2$ products were obtained without the addition of $AlCl_3$.

When NaCl is substituted for $AlCl_3$, the obtained product comprises some irregular particles as shown in Fig. 4c and d. The sample's XRD pattern is shown in Fig. S2;† the diffraction peaks can be indexed to the mixture of β-$Co(OH)_2$ and Co_3O_4. These results confirm that the existence of Al^{3+} ions, not the Cl^- anions, is the main reason for the growth of α-$Co(OH)_2$ nanoplates.

As is known, the properties of nanomaterials depend greatly on the structures of the materials; α-$Co(OH)_2$ has been widely researched as the electrode material for supercapacitors due to its high theoretical specific capacitance. In this paper, the electrochemical properties of obtained samples were first evaluated using a three-electrode device in 1 M KOH aqueous solution. The measurements were conducted using cyclic voltammetry (CV), with the voltage window of 0–0.55 V and a scanning rate of 2–50 mV s^{-1}. The obtained CV curves are shown in Fig. 5. The CV curves are nearly symmetrical and display two pairs of redox peaks. The redox reaction peaks of $Co(OH)_2$, which come from the reversible redox processes of $Co(OH)_2/CoOOH/CoO_2$, are characteristic peaks of the electrochemical pseudocapacitors from reversible redox reactions occurring within the electro-active materials.[30,31] Fig. 5a shows the CV curves of α-$Co(OH)_2$ nanoplates and β-$Co(OH)_2$ particles at a scanning rate of 5 mV s^{-1}. The area under the CV curve for α-$Co(OH)_2$ nanoplates is apparently much larger than that of β-$Co(OH)_2$ particles, which indicates that α-$Co(OH)_2$ nanoplates have a higher specific capacitance than β-$Co(OH)_2$ particles. Fig. S3† shows the nitrogen adsorption–desorption isotherms of the samples. The surface area of α-$Co(OH)_2$ nanoplates is 93.46 m^2 g^{-1}, much higher than that of β-$Co(OH)_2$ particles (42.00 m^2 g^{-1}). The higher surface area and the plate-like nanostructures provide fast ion and electron transfer and a large reaction surface area, benefiting the electrochemical performance.[32] As shown in Fig. 5b and c, changing the scanning rate from 2 to 50 mV s^{-1} subsequently increases the current density with a small positive shift of the oxidation peak potential and a small negative shift of the reduction peak potential; this may be related to the reaction ability and the OH^- concentration at the interface between electrode and electrolyte.

Chronopotentiometry measurements confirm the suggestions. Fig. 6 shows charge–discharge curves of α-$Co(OH)_2$ nanoplates and β-$Co(OH)_2$ particles in the potential range of 0–0.55 V in 1 M KOH. From the sloped curve at the discharge current of 1 A g^{-1}, the specific capacitances of α-$Co(OH)_2$ nanoplates and β-$Co(OH)_2$ particles are calculated to be 709.1 F g^{-1} and 44.2 F g^{-1}, respectively. The specific capacitance of α-$Co(OH)_2$ nanoplates is much larger than that of β-$Co(OH)_2$ particles, confirming the suggestion rising from the CV curves. As shown in Fig. 6b, when the discharging current densities are 0.5, 1, 2, 5, 10 and 25 A g^{-1}, the specific capacitance values of the α-$Co(OH)_2$ nanoplates can be calculated from the discharge curves to be 575.5 F g^{-1}, 709.1 F g^{-1}, 669.1 F g^{-1}, 610.9 F g^{-1}, 543.6 F g^{-1} and 309.1 F g^{-1}, respectively. Fig. S4† shows the Nyquist plots of α-$Co(OH)_2$ nanoplates and β-$Co(OH)_2$ particles before charge–discharge cycling. The semicircle in the high-frequency range corresponds to the faradaic reaction.[26,30,33] It can be seen from the inset of Fig. S3† that the sample synthesized with Al^{3+} ions exhibits a much more obvious semicircle

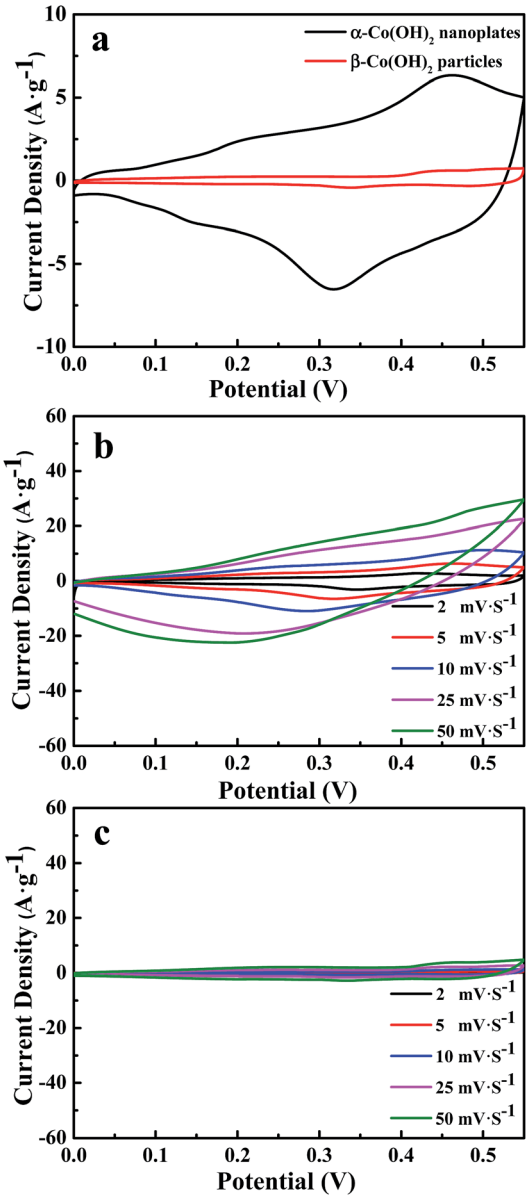

Fig. 5 CV curves in a three-electrode system of (a) α-$Co(OH)_2$ nanoplates and β-$Co(OH)_2$ particles at a scanning rate of 5 mV s^{-1}, (b) α-$Co(OH)_2$ nanoplates at a scanning rate of 2–50 mV s^{-1} and (c) β-$Co(OH)_2$ particles at a scanning rate of 2–50 mV s^{-1}.

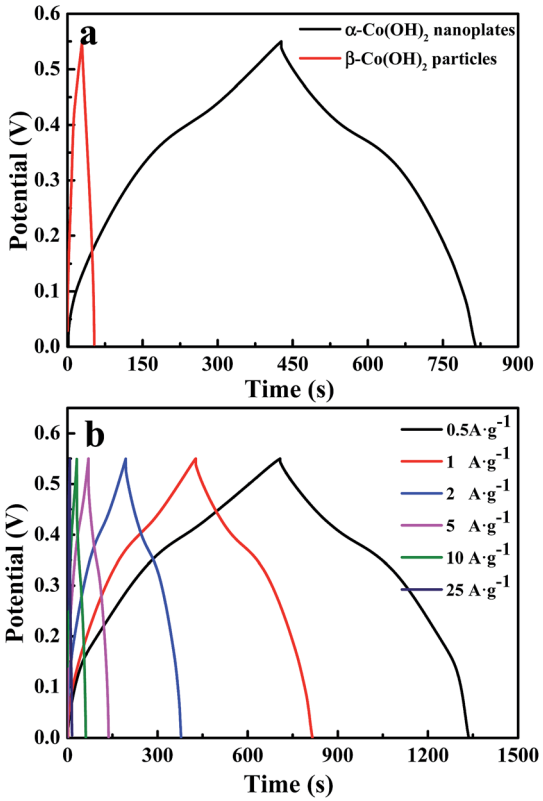

Fig. 6 Charge–discharge curves in a three-electrode system of (a) α-$Co(OH)_2$ nanoplates and β-$Co(OH)_2$ particles at a charge–discharge current density of 1 A g^{-1} and (b) α-$Co(OH)_2$ nanoplates at different current densities.

than the sample without Al^{3+} ions, which implies a much more intense faradaic reaction for Al-substituted electrodes and a longer activation process. The linear portion at lower frequency represents the Warburg impedance, and the higher slope indicates that α-$Co(OH)_2$ nanoplates possess faster ion transfer.[26]

Fig. 7a shows the Ragone plots of α-$Co(OH)_2$ nanoplates and β-$Co(OH)_2$ particles measured in 1.0 M KOH electrolyte at different current densities. The energy density is obtained as: $E = C\Delta V^2/2 \times 1000/3600$, where C is the specific capacitance value, and ΔV is the maximum testing potential, which is 0.55 V in this work. The power density is calculated as: $P = 3600E/t$, where E is energy density and t is the discharging time (s).[21,34,35] As shown in Fig. 7a, the power density increases from 275 to 6875 W kg^{-1} when energy density decreases from 29.8 to 13.0 W h kg^{-1} for α-$Co(OH)_2$ nanoplates, while the energy density decreases from 2.0 to 0.4 W h kg^{-1} for β-$Co(OH)_2$ particles. Based on the result, we can see that the α-$Co(OH)_2$ nanoplate electrode is capable of delivering high power without remarkable loss in energy, indicating its promising application in supercapacitors. Compared with these two electrode materials, α-$Co(OH)_2$ nanoplates possess much higher energy than β-$Co(OH)_2$ particles at the same power density, which is consistent with the result of charge–discharge curves.

For practical applications, long cycle life is a very important factor of supercapacitors; thus, the cycle charge–discharge test was employed to examine the service life of α-$Co(OH)_2$ nanoplates. Fig. 7b gives the variation of specific capacitance with cycle number to 1000 cycles at a constant current density of 5 A g^{-1} in 1.0 M KOH electrolyte. The capacitance of α-$Co(OH)_2$ nanoplates reaches a high value of 498.2 F g^{-1} at the first cycle, and it gradually comes down to 477.3 F g^{-1}, a 95.8% retention of the initial capacitance, while β-$Co(OH)_2$ particles reach 32.9 F g^{-1} at the first cycle and then 31.9 F g^{-1}, a 96.9% retention of the initial capacitance. This result reveals that α-$Co(OH)_2$ nanoplates and β-$Co(OH)_2$ particle electrodes all have good cycle properties, but the β-$Co(OH)_2$ particle electrode has lower

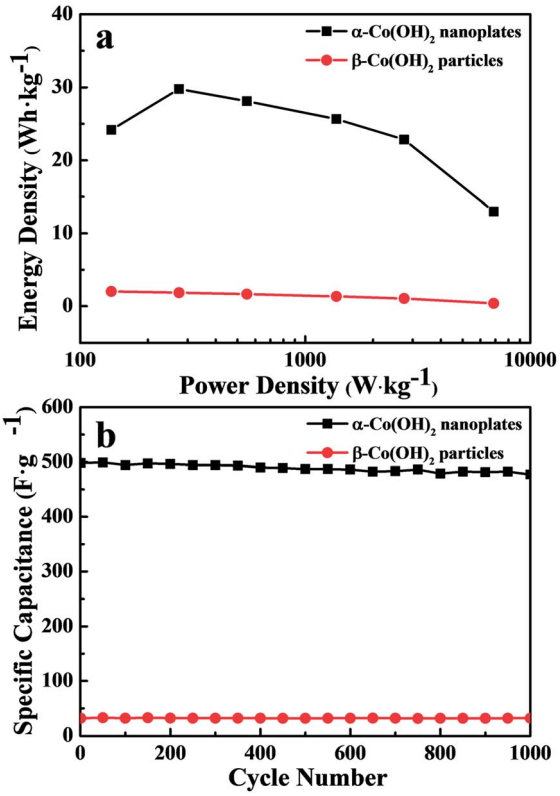

Fig. 7 (a) Ragone plot of the electrode made from the samples at different current densities and (b) cycling properties of the samples at current density of 5 A g^{-1}.

capacitance properties, so α-$Co(OH)_2$ nanoplates can serve as a better electrode material for electrochemical capacitors.

The water oxidation activities of α-$Co(OH)_2$ nanoplates were evaluated by steady-state electrochemistry measurements in 1 M KOH aqueous solutions using a typical three-electrode device. As shown in Fig. 8a, the polarization curve recorded with the α-$Co(OH)_2$ nanoplates reveals a markedly small onset potential of 1.51 V for the OER, beyond which the anodic current rises fast by applying a smaller overpotential. In contrast, β-$Co(OH)_2$ particles shows an inferior OER activity with a larger onset potential of 1.59 V and slower current increase. The mass activity of α-$Co(OH)_2$ nanoplates is 28.2 A g^{-1} at a quite small overpotential of 348 mV, while it is only 0.2 A g^{-1} for β-$Co(OH)_2$ particles (see Fig. 8b and Table S1†). The overpotential of 449 mV at 10 mA cm^{-2} for β-$Co(OH)_2$ particles is evidently higher than that of α-$Co(OH)_2$ nanoplates (Table S1†). The α-$Co(OH)_2$ nanoplates also exhibit a linear increase in TOF with overpotential, affording much higher TOFs than β-$Co(OH)_2$ particles (inset of Fig. 8b). The above results demonstrate that α-$Co(OH)_2$ nanoplates have an excellent catalytic water oxidation activity, remarkably outperforming β-$Co(OH)_2$ particles. The water oxidation activities are related to the electronic property of α-$Co(OH)_2$ nanoplates. Electrochemical impedance characterization was used to determine the electronic property. Fig. 8c reveals a decreased transport resistance of α-$Co(OH)_2$ nanoplates (inset of Fig. 8c).

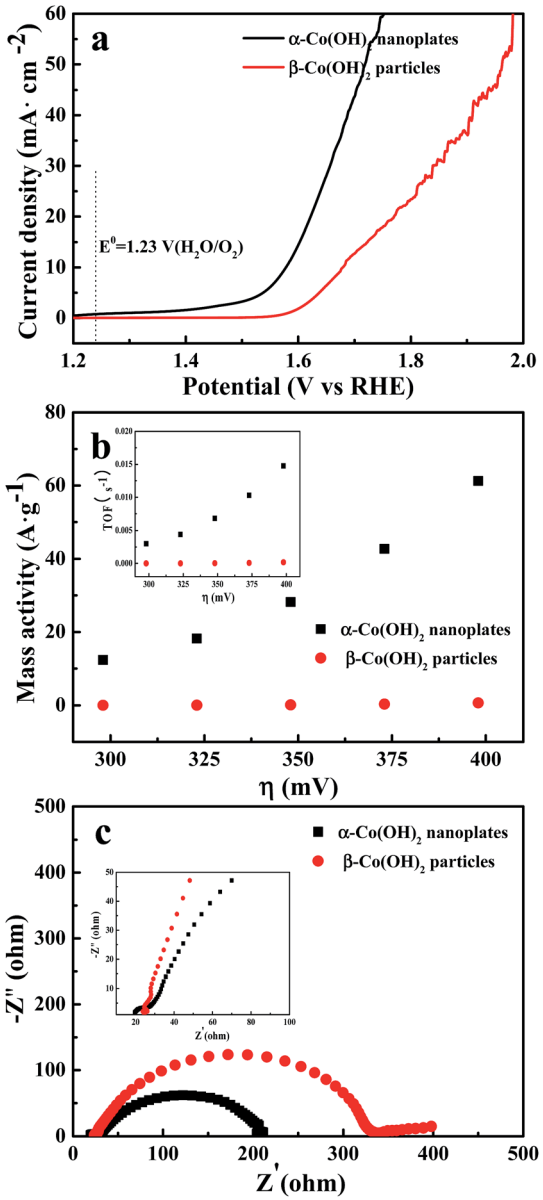

Fig. 8 (a) Polarization curves, (b) mass activities and TOFs (inset) and (c) electrochemical impedance spectra of α-$Co(OH)_2$ nanoplates and β-$Co(OH)_2$ particles.

Conclusions

In summary, α-$Co(OH)_2$ nanoplates were synthesized by using metal ions of Al^{3+} as a structure-inducing agent through hydrothermal method. As electrode materials for supercapacitors, the α-$Co(OH)_2$ nanoplates exhibit a good capacitive property of 709.1 F g^{-1} at the current density of 1 A g^{-1} and a long cycle life, maintaining 95.8% of the initial capacity at the current density of 5 A g^{-1} after 1000 cycles. The α-$Co(OH)_2$ nanoplates also can effectively oxidize water with excellent OER activity, with a small overpotential of 348 mV at the current density of 10 mA cm^{-2} and large mass activity of 28.2 A g^{-1}. These results provide a new and facile approach to fabricating

high-performance electrodes for supercapacitors and water oxidation electrocatalysts.

Experimental section

Preparation of α-$Co(OH)_2$ nanoplates

In a typical procedure, the starting solution was prepared by adding 0.4982 g of $CoAc_2$ (analytically pure) in 20 mL of 0.025 M aluminum chloride solution under magnetic stirring. Then, 2 mL of ammonia solution (25%, analytically pure) was added. After 10 min of stirring, the mixture was transferred to and sealed in a 50 mL Teflon-lined autoclave, kept at 120 °C for 6 h, and finally cooled to room temperature. The precipitate was collected by centrifugation (6000 rpm, 1 min), washed alternately with deionized water and ethanol, and dried in air under ambient conditions.

Characterizations

Powder X-ray diffraction (XRD) patterns were collected using a Bruker D8 ADVANCE diffractometer with Cu Kα radiation (λ = 1.5418 Å) from $2\theta = 5$–80°. Scanning electron microscopy (SEM) characterizations were performed on Hitachi S-4800 at 5 kV. Transmission electron microscopy (TEM) images were obtained using a JEOL JEM-2100 transmission electron microscope operating at 200 kV. X-ray photoelectron spectra (XPS) were collected on an ESCALab MKII X-ray photoelectron spectrometer, using nonmonochromatized Al Kα X-ray as excitation source. The binding energies were corrected for specimen charging by calibrating the C 1s peak to 284.6 eV. Raman spectra were recorded on an RM2000 Raman microscope from Renishaw Scientific with a 514 nm solid laser as excitation source. The specific surface areas of the samples were measured by using nitrogen sorption–desorption at 77 K on a surface area analyzer (Micromeritics TriStar 3000, USA) and calculated with the BET method.

Electrochemical measurements

Supercapacitors measurements. A three-electrode system was used to measure the electrochemical properties of the as-prepared α-$Co(OH)_2$ nanoplates, in which α-$Co(OH)_2$ nanoplates were used as the working electrode, platinum wire as the counter electrode, and a standard calomel electrode (SCE) as the reference electrode in 1 M KOH aqueous solution as electrolyte. The working electrode was prepared by mixing 80 wt% of electroactive material, 10 wt% of acetylene black, 10 wt% of polytetrafluoroethylene and a few drops of isopropyl alcohol as a solvent. This mixture was then coated onto the foamed nickel electrode and dried at 60 °C for 12 h. The electrochemical performance measurements were carried out on a CHI 660e electrochemical workstation. Cycle voltammetry (CV) and galvanostatic charge–discharge tests were used to determine the electrochemical properties of the electrodes.

Oxygen evolution reaction measurements. All measurements were carried out at room temperature. The modified electrode was prepared as follows: 0.004 g of electrocatalyst powder was dispersed in 1.5 mL DI-water and 0.5 mL ethanol mix solvent with 60 μl 5% Nafion. Then, 10 μL of the solution was dropped onto the surface of a glassy carbon electrode ($r = 3$ mm) and left to dry in air for 12 h. The electrochemical measurements were all carried out on a CHI660e electrochemical workstation with a conventional three-electrode electrochemical cell. A GC electrode modified with electrocatalyst powder was used as working electrode, saturated Ag/AgCl as the reference electrode and a platinum wire as the counter electrode. All the electrochemical measurements were conducted in 1 M KOH electrolytes bubbled with oxygen for 30 min in order to ensure H_2O/O_2 equilibrium at 1.23 V *versus* the reversible hydrogen electrode (RHE). The polarization curves were measured at a sweep rate of 5 mV s^{-1}. Electrochemical impedance spectroscopy (EIS) data were recorded with a frequency range of 0.01–1000 kHz at a bias potential of 1.6 V *vs.* RHE.

Acknowledgements

This work was supported by the National Natural Science Foundation of China (No. 21301002, 51302001), Anhui Province College Excellent Young Talents Fund (No. 2013SQRL037ZD and 2013SQRL036ZD), Excellent Young Talents Support Plan of Anhui Province College and the Outstanding Young Scientists Program of Anhui Polytechnic University (No. 2015JQ03 and 2015JQ02).

Notes and references

1 L. Cao, F. Xu, Y. Y. Liang and H. L. Li, *Adv. Mater.*, 2004, **16**, 1853–1857.
2 V. Gupta, T. Kusahara, H. Toyama, S. Gupta and N. Miura, *Electrochem. Commun.*, 2007, **9**, 2315–2319.
3 T. Zhao, H. Jiang and J. Ma, *J. Power Sources*, 2011, **196**, 860–864.
4 W. J. Zhou, J. Zhang, T. Xue, D. D. Zhao and H. L. Li, *J. Mater. Chem.*, 2008, **18**, 905–910.
5 F. Song and X. L. Hu, *Nat. Commun.*, 2014, **5**, 4477–4485.
6 C. Z. Yuan, L. R. Hou, L. F. Shen, D. K. Li, F. Zhang, C. G. Fan, J. M. Li and X. G. Zhang, *Electrochim. Acta*, 2010, **56**, 115–121.
7 M. Aghazadeh, H. MohammadShiri and A. A. M. Barmi, *Appl. Surf. Sci.*, 2013, **273**, 237–242.
8 M. Li, S. H. Xu, T. Liu, F. Wang, P. X. Yang, L. W. Wang and P. K. Chu, *J. Mater. Chem. A*, 2013, **1**, 532–540.
9 J. Jiang, A. L. Zhang, L. L. Li and L. H. Ai, *J. Power Sources*, 2015, **278**, 445–451.
10 X. X. Zou, A. Goswami and T. Asefa, *J. Am. Chem. Soc.*, 2013, **135**, 17242–17245.
11 Z. Y. Jiang, Q. Kuang, Z. X. Xie and L. S. Zheng, *Adv. Funct. Mater.*, 2010, **20**, 3634–3645.
12 R. M. Liu, Y. W. Jiang, H. Fan, Q. Y. Lu, W. Du and F. Gao, *Chem.–Eur. J.*, 2012, **18**, 8957–8963.
13 G. Liu, J. C. Yu, G. Q. Lu and H. M. Cheng, *Chem. Commun.*, 2011, **47**, 6763–6783.
14 Y. Z. Zhang, Y. Wang, Y. L. Xie, T. Cheng, W. Y. Lai, H. Pang and W. Huang, *Nanoscale*, 2014, **6**, 14354–14359.
15 W. X. Niu, L. Zhang and G. B. Xu, *ACS Nano*, 2010, **4**, 1987–1996.

16 L. J. Yang, X. P. Gao, Q. D. Wu, H. Y. Zhu and G. L. Pan, *J. Phys. Chem. C*, 2007, **111**, 4614–4619.
17 J. C. Huang, D. X. Cao, T. Lei, S. Yang, X. B. Zhou, P. P. Xu and G. L. Wang, *Electrochim. Acta*, 2013, **111**, 713–719.
18 M. J. Zhou, L. L. Cai, M. Bajdich, M. García-Melchor, H. Li, J. J. He, J. Wilcox, W. D. Wu, A. Vojvodic and X. L. Zheng, *ACS Catal.*, 2015, **5**, 4485–4491.
19 J. C. Huang, T. Lei, X. P. Wei, X. W. Liu, T. Liu, D. X. Cao, J. L. Yin and G. L. Wang, *J. Power Sources*, 2013, **232**, 370–375.
20 S. Gao, Y. F. Sun, F. C. Lei, L. Liang, J. W. Liu, W. T. Bi, B. C. Pan and Y. Xie, *Angew. Chem.*, 2014, **126**, 13003–13007.
21 M. Aghazadehn, S. Dalvand and M. Hosseinifard, *Ceram. Int.*, 2014, **40**, 3485–3493.
22 F. Y. Zhou, Q. L. Liu, J. J. Gu, W. Zhang and D. Zhang, *Electrochim. Acta*, 2015, **170**, 328–336.
23 H. W. Wang, H. T. Tan, H. Yi, Y. Zhang, G. L. Guo, X. F. Wang, S. Madhavi and Q. Y. Yan, *RSC Adv.*, 2015, **5**, 88191–88201.
24 J. H. Huang, J. T. Chen, T. Yao, J. F. He, S. Jiang, Z. H. Sun, Q. H. Liu, W. R. Cheng, F. C. Hu, Y. Jiang, Z. Y. Pan and S. Q. Wei, *Angew. Chem.*, 2015, **127**, 8846–8851.
25 R. M. Liu, Z. X. Jiang, Q. Liu, X. D. Zhu and W. Y. Chen, *CrystEngComm*, 2015, **17**, 4449–4454.
26 J. Tang, D. Q. Liu, Y. X. Zheng, X. W. Li, X. H. Wang and D. Y. He, *J. Mater. Chem. A*, 2014, **2**, 2585–2591.
27 V. Gupta, S. Gupta and N. Miura, *J. Power Sources*, 2008, **177**, 685–689.
28 F. Song and X. L. Hu, *J. Am. Chem. Soc.*, 2014, **136**, 16481–16484.
29 Z. P. Liu, R. Z. Ma, M. Osada, K. Takada and T. Sasaki, *J. Am. Chem. Soc.*, 2005, **127**, 13869–13874.
30 M. J. Jing, Y. C. Yang, Y. R. Zhu, H. S. Hou, Z. B. Wu and X. B. Ji, *Electrochim. Acta*, 2014, **141**, 234–240.
31 Y. F. Tang, Y. Y. Liu, S. X. Yu, S. C. Mu, S. H. Xiao, Y. F. Zhao and F. M. Gao, *J. Power Sources*, 2014, **256**, 160–169.
32 F. X. Wang, Z. C. Liu, X. W. Wang, X. H. Yuan, X. W. Wu, Y. S. Zhu, L. J. Fu and Y. P. Wu, *J. Mater. Chem. A*, 2016, **4**, 5115–5123.
33 W. L. Ma, J. Y. Xue and H. T. Cui, *Ionics*, 2016, **22**, 573–579.
34 Y. Shi, S. Tian, Y. H. Chen, Y. P. Wu and R. Holze, *J. Power Sources*, 2009, **194**, 1222–1225.
35 Q. T. Qu, L. Li, S. Tian, W. L. Guo, Y. P. Wu and R. Holze, *J. Power Sources*, 2010, **195**, 2789–2794.